Journal of Rare Earths 36 (2018) 1074–1083

Contents lists available at ScienceDirect

Journal of Rare Earths

journal homepage: http://www.journals.elsevier.com/journal-of-rare-earths

Characterization and electrochemical performance of CeO_2 and Eu-doped CeO_2 films as a manganese redox flow battery component

Mônica A. Rodrigues [a], Ariadne C. Catto [b], Elson Longo [c], Edson Nossol [a], Renata C. Lima [a, *]

[a] Institute of Chemistry, Federal University of Uberlândia, 38400-902, Uberlândia, MG, Brazil
[b] Institute of Chemistry, São Paulo State University, P.O. Box 355, 14801-907, Araraquara, SP, Brazil
[c] LIEC, Department of Chemistry, Federal University of São Carlos, 13565-905, São Carlos, SP, Brazil

ARTICLE INFO

Article history:
Received 24 November 2017
Received in revised form
26 April 2018
Accepted 17 May 2018
Available online 8 June 2018

Keywords:
Cerium oxide
Europium
Nanoparticles
Electrochemical properties
Batteries
Rare earths

ABSTRACT

Hexagonal CeO_2 and Eu-doped CeO_2 nanoparticles were obtained using a facile microwave-hydrothermal method under mild conditions and their application towards manganese redox flow battery component were studied. The structural properties were studied by X-ray diffraction and indicate that samples present a fluorite structure. Raman spectroscopy shows Eu^{3+} ions substitute Ce^{4+} and generate oxygen vacancies. Electrochemical properties of pure and Eu-doped CeO_2 films deposited at graphite substrates investigated by cyclic voltammetry and galvanostatic charge–discharge indicate that dopant concentration affects the electrochemical properties of CeO_2. The increase in the reversibility redox of electrochemical systems observed is attributed to coexistence of Ce^{4+}/Ce^{3+} redox couple confirmed by XPS. Charge–discharge tests display coulombic and voltage efficiency values of above 80% and 90%, respectively. The obtained specific capacity for $Ce_{0.99}Eu_{0.01}O_2$ (372.49 mAh/g) and pure oxide (334.84 mAh/g) indicates that both samples are promising for application in Mn-batteries.

1. Introduction

Nanosized cerium oxide (CeO_2) particles have attracted great attention from scientific community due the coexistence of Ce^{4+} and Ce^{3+} ions and the presence of oxygen vacancies, that provide a good ionic conductivity and a high capacity for store and exchange oxygen.[1–5] These intrinsic defects give CeO_2 physical and chemical properties of great scientific and technological interest, thus rendering this material the characteristic of one of the most studied rare earth oxides.[1,6]

Various studies indicate that insertion of lower valence ions, such as Eu^{3+}, Er^{3+} and Sm^{3+} onto the oxide crystalline lattice potentiates the intrinsic properties, since the substitution of Ce^{4+} ions by trivalent cations increases the number of oxygen vacancies, in addition to inserting new energy levels into its structure.[7–12] Therefore, both pure and Eu-doped CeO_2 possess various applications in catalysis,[13–15] gas and humidity sensors,[16,17] pigments[18] and optoelectronic devices. When dealing with its electrochemical properties and applications, cerium oxide presents great potential, as it can be used in electro-catalysis for oxidation of alcohols,[19,20] in super-capacitors with high specific capacity[21–23] or as cathode/anode component in lithium ion batteries.[24–28]

Michalska and collaborators[29] reported that modification of $LiMn_2O_4$ electrodes with low concentration of CeO_2 resulted in coulombic efficiency increasing in the first charge–discharge cycle: 82% and 89% for the $LiMn_2O_4$ and CeO_2 modified electrodes, respectively. In addition, a significant improvement was also noted in the cycling stability and retention capacity for CeO_2 modified electrode. The unmodified cathode presented 90% of the first discharge capacity, while the $LiMn_2O_4/CeO_2$ electrode retained 98% after 100 charge–discharge cycles, indicating that the addition of oxide significantly changes the electrochemical properties of the material. Liu and Le[30] prepared CeO_2 electrodes containing 80% of the oxide, 12% of acetylene black and 8% of polytetrafluoroethylene and evaluated their performance as anodes for lithium ion batteries. The results showed an excellent specific discharge capacity in the first cycle (529 mAh/g), thus providing reversible stabilization at around 374 mAh/g after 50 cycles. Although lithium ion batteries

Foundation item: Project supported by the Coordenação de Aperfeiçoamento de Pessoal de Nível Superior (Capes), Conselho Nacional de Desenvolvimento Científico e Tecnológico (CNPq), Fundação de Amparo à Pesquisa do Estado de Minas Gerais (FAPEMIG), Rede Mineira de Química (RQ-MG) and Grupo de Materiais Inorgânicos do Triângulo - GMIT Research Group supported by FAPEMIG (APQ-00330-14).

* Corresponding author. Fax: +55 34 3239 4143.
E-mail address: rclima@ufu.br (R.C. Lima).

https://doi.org/10.1016/j.jre.2018.05.004
1002-0721/

are very efficient and widely used, their high cost, toxicity and difficulty of access to reserves of Li^+ are considerable disadvantages. For these reasons, the construction of batteries based on others alkali metals or transition ions, such as sodium, vanadium and manganese has been extensively studied.[26,31–41]

In this context, great efforts have been done in order to develop new types of redox flow batteries (RFB), especially regarding the development of new electrodes and substitution of vanadium based electrolyte system. The use of the Mn^{2+}/Mn^{3+} system as redox couple and graphite as the working electrode in acid medium was investigated by Xue and collaborators.[36] High coulombic (69.4%) and voltage efficiency (90.4%) values were obtained, confirming the applicability of the system for the use in this type of batteries. Lipka and Swartz reported the construction of a manganese ions hybrid flow batteries. The mentioned work involved a hybrid flow battery system that use Mn^{2+} and Mn^{3+} species in the anolyte and Mn^{2+} and Mn^0 species in the catholyte, and the electrolyte was composed by ammonium sulfate and sulfuric acid.[42] Sleightholme and collaborators[43] studied a non-aqueous manganese acetylacetonate electrolyte for RFB. In these batteries the quasi-reversible redox process involves Mn^{2+}/Mn^{3+} and Mn^{3+}/Mn^{4+} redox couples. The coulombic efficiencies increased from 74% for cycle 3 and 97% for cycle 10. He and collaborators[44] reported that introduction of manganese in vanadium redox flow cell generates a battery with good coulombic and energy efficiency (95% and 84%, respectively) after 40 g alvanostatic charge-discharge cycles, with a discharge capacity above 4000 mAh. In addition, the obtained energy density of V/Mn RFB (17.85 W/h) was higher than all vanadium cells.

Due to the great electrochemical potential of cerium oxide as electrode and Mn^{2+}/Mn^{3+} couple along with the necessity to develop batteries with lower cost and toxicity, this work presents a system constituted of manganese ions as redox couple and CeO_2 films as electrode. The oxide films were prepared using pure and Eu-doped CeO_2, with the influence of Eu^{3+} ions in the electrochemical properties of pure oxide investigated by cyclic voltammetry and galvanostatic charge–discharge tests. Additionally, the samples were rapidly obtained by microwave-assisted hydrothermal (MAH) method,[3,45–48] and the effect of Eu^{3+} ions in the CeO_2 lattice was investigated by X-ray diffraction (XRD), X-ray photoelectron spectroscopy (XPS), Raman spectroscopy, field emission gun scanning electron microscopy (FEG-SEM) and transmission electron microscopy (TEM). The surface area and pore size distribution were also determinate.

2. Material and methods

2.1. Synthesis of $Ce_{1-x}Eu_xO_2$ oxides

Pure CeO_2 was obtained from the addition of 1.0091 g of $Ce(NO_3)_2 \cdot 6H_2O$ in 40 mL of distilled water under constant stirring. KOH solution (3.0 mol/L) was added until pH = 11. Eu-doped CeO_2 samples resulted from the addition of $Eu(NO_3)_3 \cdot 6H_2O$ in different molar ratios in relation to Ce^{4+} ($x = 0.01$ and 0.04 mol Eu^{3+} ions). The final solutions were transferred into a Teflon autoclave and then sealed and placed in an microwave-hydrothermal equipment. The solutions remained in an autoclave for 4 min at 100 °C. The precipitated powder was washed several times with deionized water and ethanol. Finally, the powder samples were dried at 80 °C for 2 h in air atmosphere.

2.2. Graphite substrate preparation

Graphite substrates were prepared by the use of graphite bars (0.75 cm^2) extracted from commercially purchased pencils. All graphite bars were polished using Al_2O_3 powder (0.3 μm) and distilled water to guarantee the homogeneity of the surface before the films deposition. After polishing, the graphite substrates were washed several times with distilled water and acetone under ultrasound bath. Lastly, the substrates were dried at 100 °C for 2 h in air atmosphere.

2.3. CeO_2 and Eu-doped CeO_2 films preparation

The films were prepared by the interfacial method.[49–51] Briefly, this method consists in the addition of 3.0 mg of the oxides in 20 mL of distilled water under magnetic stirring for 30 min, followed by ultrasound bath for 30 more minutes. The resulting dispersion was transferred to a 50 mL round-flask containing 20 mL of toluene under magnetic stirring, with consequent formation of a two-phase system. After 24 h, the magnetic stirring was interrupted and a thin film was obtained in the liquid–liquid interface. To deposit the films on the graphite substrates surface, the two-phase system containing the interfacial film was added to a beaker containing the substrates previously prepared. Lastly, using tweezers, the graphite substrates were pulled against the interface for film deposition. The films were dried at 70 °C for 2 h in air atmosphere.

2.4. Physical characterization

CeO_2 powders were characterized by X-ray diffraction (Shimadzu XRD 6000) with a Cu Kα radiation source ($\lambda = 0.15406$ nm). The structure was refined using the Rietveld method and the General Structure Analysis System (GSAS) package, with an EXPGUI graphical user interface.[52] Raman spectra were recorded at room temperature using a HORIBA Scientific's Raman spectrometer (LabRAM HR Evolution microscope) with 1 mm resolution and a 532 nm argon ion laser with an incidence power of 2 mW. Scanning electron microscope (SEM) and transmission electron microscopy (TEM) images were obtained using a field emission gun (FEG) (TESCAN, BrnoKohoutovice, Czech Republic) operated at 10 kV, and FEI American, Tecnai G2TF20) operating at 25 kV, respectively. The micro-analysis by energy-dispersive X-ray (EDX) spectroscopy was performed using an Oxford Instruments system, operating at 20 kV. X-ray photoelectron spectroscopy (XPS) analyses were performed on a Scienta Omicron, model ESCA ± spectrometer using monochromatic Al Kα (1486.6 eV) radiation. Peak decomposition was performed using a Gaussian–Lorentzian line shape with a Shirley nonlinear sigmoid-type baseline. The binding energies were corrected for charging effects by assigning a value of 284.8 eV to the adventitious C 1s line. The data were analyzed using Casa XPS software (Casa Software Ltd., U.K.). The N_2 adsorption–desorption isotherms were performed at −196 °C using a NOVAtouch surface area and pore-size analyzer with Quantachrome TouchWin software (version 1.1.). Specific surface area was calculated using the Brunauer, Emmett and Teller method (BET) and the Barrett, Joyner and Halenda (BJH) method was used to calculate the pore size distribution.[53,54] All powders were degassed in vacuum at 150 °C during 10 h for the surface area determination.

2.5. Electrochemical studies

Cyclic voltammetry (CV) and galvanostatic charge–discharge analyses were carried out using a PGSTAT12 Autolab potentiostat. Experiments were conducted in a conventional one-compartment three-electrode cell containing the working CeO_2 film electrode, a graphite rod as a counter electrode and an Ag/AgCl (3.0 mol/L KCl) electrode as reference. Electrochemical tests for evaluation of CeO_2 films as Mn-battery component were measured using as electrolyte

an aqueous solution of manganese sulfate (0.3 mol/L) and sulfuric acid (1.0 mol/L). Cyclic voltammetry (CV) tests were obtained at a scan rate of 5.0 mV/s in the potential range of 0.4–1.5 V. Galvanostatic charge–discharge measurements were carried out in the potential range of 0.9–1.5 V. All the experiments were performed at ambient temperature.

3. Results and discussion

3.1. Characterization studies

The XRD patterns of pure and doped CeO_2 samples refined by the Rietveld method are presented in Fig. 1(a). All diffraction peaks were indexed according to the face-centered cubic structure of CeO_2 with lattice constant $a = b = c = 0.541$ nm (JCPDS 34-0394). Eu-doped CeO_2 samples present a single pure phase with a fluorite structure ($fm3m$ space group), without formation of secondary phases. The FWHM (full width at half maximum) values (Fig. 1(b)) referring to [111] lattice planes of *fcc* CeO_2 indicate a decrease in crystallinity associated with the insertion of Eu^{3+} ions in the oxide lattice.

The peak position (2θ) was shifted to lower angles values in comparison to pure CeO_2. According to Pikalova and collaborators,[55] this fact can be assigned to insertion of dopant with larger ionic radius (0.1066 nm for Eu^{3+}) when compared to Ce^{4+} ions (0.0970 nm). This behavior can be ascribed to the insertion of Eu^{3+} ions in the CeO_2 matrix, substituting Ce^{4+} ions and creating oxygen vacancies in the ceria crystal structure, as reported by Sahoo and collaborators.[56] Moreover, the broadening peaks also can be attributed to crystallite size decrease. Debye–Scherrer formula was used to estimate the crystallite size of all CeO_2 samples.[57,58] The crystallite size decreased with the insertion of Eu into CeO_2 lattice,[58] as shown in Table 1.

Table 1 displays the data obtained after Rietveld refinement. The χ^2 and profile parameters (R_p, R_{wp}) values indicate a high quality of refinement. The change in lattice parameters and cell volume expansion indicates that Eu^{3+} ions were incorporated in the CeO_2 matrix occupying preferentially the Ce^{4+} position rather than interstitial sites.[9,55,59,60]

FEG-SEM and TEM images of the pure CeO_2 and Eu-doped CeO_2 samples are shown in Fig. 2(a–c). Electron microscopy images show that samples exhibited hexagonal shape morphology with a significant particle agglomeration level. TEM images and the respective histograms related with the average particle size distributions of the pure CeO_2 and Eu-doped CeO_2 samples are presented in Fig. 2(a–c). It can be observed that all samples exhibited a uniformity of size distribution, ranging from 12 to 5 nm for pure CeO_2 and $Ce_{0.99}Eu_{0.01}O_2$ samples, respectively. In addition, the presence of characteristic elements of materials are confirmed by EDX spectra shown in Fig. 2(a–c), indicating the presence of europium in the doped CeO_2 samples. The peaks observed for silicon (Si) element were derived from the substrates used in the samples preparation to EDX analysis.

This method is widely used for presenting a uniform heating which provides a good control in the formation of homogeneous particles with reduced preparation time when compared to conventional hydrothermal method. Besides this characteristic, MAH method is environmentally friendly, easy to operate and supports the growth of particles in nanometer size.[46,61–63]

Raman spectra of CeO_2 samples are shown in Fig. 3. Pure CeO_2 sample presented an intense band at around 464 cm^{-1} corresponding to F_{2g} mode, which is characteristic of CeO_2 cubic structure.[64] This F_{2g} mode is attributed to the symmetric vibration of oxygen atoms around the Ce^{4+}. Two small bands are observed for all samples: a band near to 600 cm^{-1} can be attributed to O_h vibrational mode, assigned to existence of intrinsic oxygen vacancies in the oxide structure, and other band at around 1050 cm^{-1}, attributed to the primary A_{1g} asymmetry, combined with small additional contributions from E_g and F_{2g} symmetries.[58,65,66] For both doped samples were observed the broadening and shift of the F_{2g} vibrational mode to lower wavenumbers, 459 and 463 cm^{-1} for $Ce_{0.99}Eu_{0.01}O_2$ and $Ce_{0.96}Eu_{0.04}O_2$, respectively. This displacement occurs due to changes in the lattice parameters, with increase of oxygen vacancies concentration and decrease of nanoparticle size caused by the insertion of Eu^{3+} ions.[9] Additionally, Raman spectra of doped oxides presented a band around 530 cm^{-1}, which is more evident for the sample with larger amount of Eu^{3+} dopant.[67] This band is assigned to the increase of punctual defects in the oxide structure caused by extrinsic oxygen vacancies generated by the presence of Eu^{3+} ions.[9,58,67] Hernández and collaborators[9] observed the same behavior for rare earth ions doped CeO_2. The authors reported that insertion of La^{3+}, Gd^{3+} and Eu^{3+} ions in CeO_2 lattice causes losses in selection rule for Raman scattering and, consequently, phonons at all parts in the Brillouin zone contribute to the optical spectra and modifications in the width and position of F_{2g} mode besides new bands may occur between 500 and 600 cm^{-1}.[68] The Raman modes observed for CeO_2 samples are in accordance to XRD patterns, indicating the obtained structure and purity of the samples.

Fig. 4(a) shows the XPS survey spectra of the pure and doped CeO_2 samples. The peaks in these spectra were indexed and

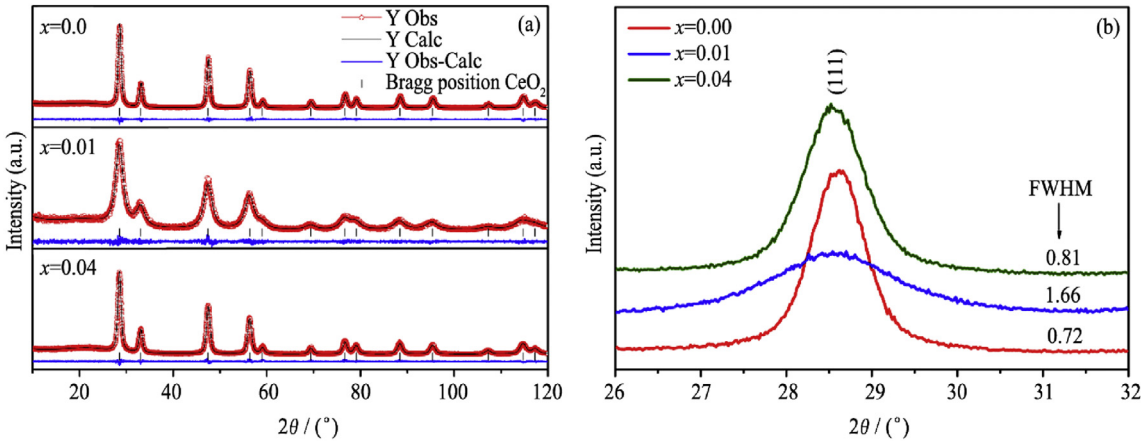

Fig. 1. (a) Rietveld refinement plots for $Ce_{1-x}Eu_xO_2$ samples obtained by the MAH method (x = mol of Eu^{3+} ions); (b) Extended region of X-ray diffractograms.

Table 1
Parameters obtained from Rietveld refinement method and crystallite size values calculated for $Ce_{1-x}Eu_xO_2$ samples (x = mol of Eu^{3+} ions).

Samples	Crystallite size (nm)	Cell parameters		R_{wp} (%)	R_p (%)	R_{bragg} (%)	χ^2
		$a = b = c$ (nm)	V (10^{-3} nm^3)				
0.0	11.7	0.54144(18)	158.733(16)	5.48	4.30	1.93	1.16
0.01	4.9	0.54271(51)	159.849(46)	6.19	4.93	1.12	1.09
0.04	10.1	0.54165(27)	158.913(24)	5.62	4.37	1.78	1.19

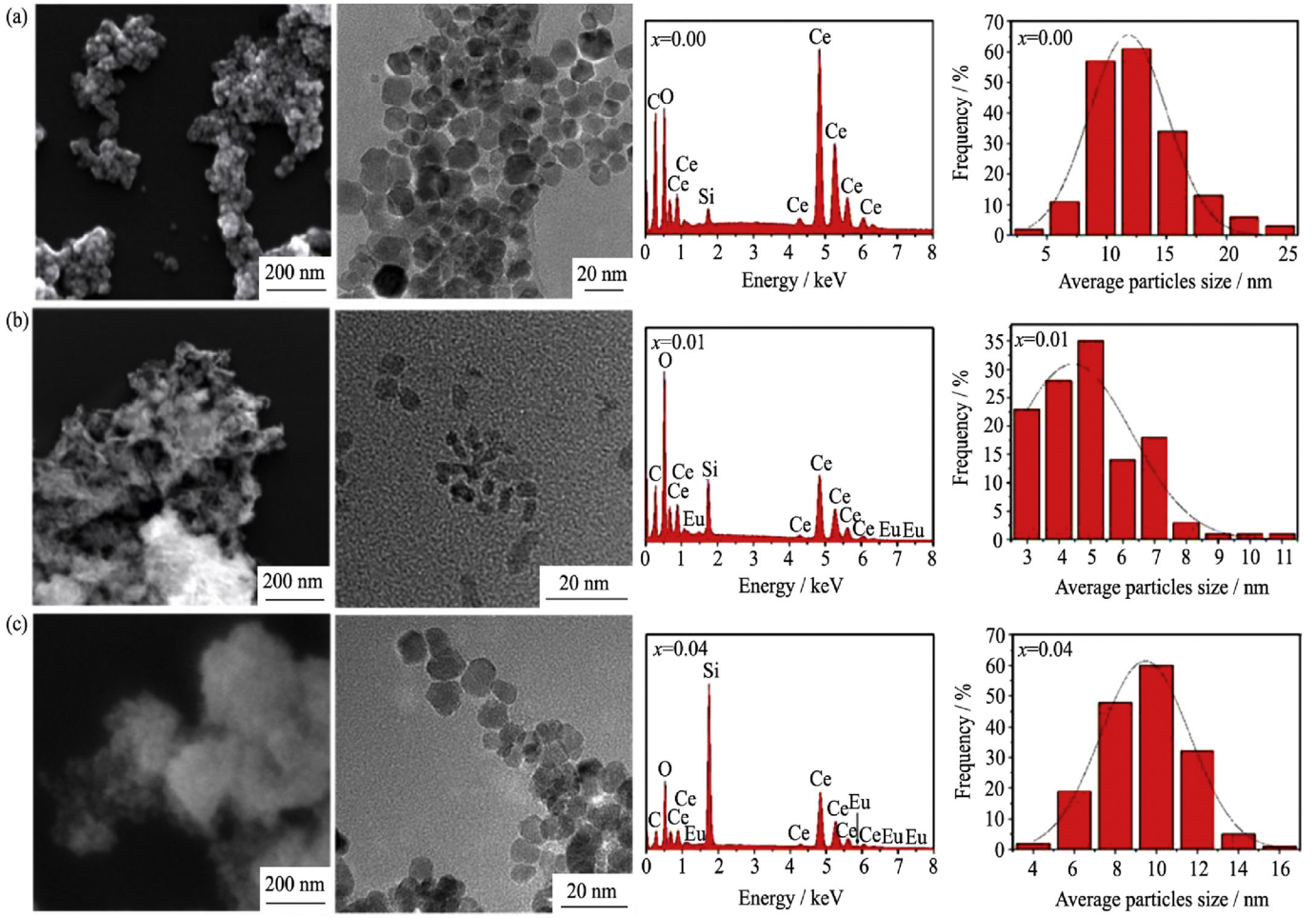

Fig. 2. FEG-SEM and TEM images of the $Ce_{1-x}Eu_xO_2$ samples (x = mol of Eu^{3+} ions). (a) $x = 0.0$; (b) $x = 0.01$; (c) $x = 0.04$. EDX spectra and histograms are presented on the right side of the corresponding microscopy images.

revealed the presence of Ce, O, and C; however, it was not possible to detect the presence of europium in the doped CeO_2 samples due to low concentration of this element, which limits the use of this technique. In order to confirm the presence of characteristic elements of materials the EDX analysis was performed, indicating the presence of europium in the doped CeO_2 samples.

In the high-resolution Ce 3d XPS spectra shown in Fig. 4(b), a spin–orbit components were observed, in which each spin–orbit component (Ce $3d_{3/2}$ and Ce $3d_{5/2}$) is further split by multiplet splitting. As can be observed the Ce 3d spectra contain three individual doublets associated to Ce^{4+} cations and two spin–orbit doublets associated to Ce^{3+} cations,[69] suggesting the coexistence of Ce^{3+} and Ce^{4+} in all samples. A comparison of the high resolution Ce 3d XPS spectra of the samples shows that the pure sample exhibits a higher contribution of the components associated with the Ce^{3+} cations, while the europium addition contributed to increase of the fraction of the Ce^{4+} state.

Fig. 4 (c) shows the high-resolution Eu 3d XPS spectra. It is possible to observe the presence of weak peaks associated to spectral doublet Eu $3d_{3/2}$ and Eu $3d_{5/2}$ with binding energies of about 1166.4 and 1134.1 eV, respectively. The values of BE are consistent with the Eu trivalent state taken from literature.[70,71] As can be observed in Fig. 4 (c), the Eu $3d_{3/2}$ and Eu $3d_{5/2}$ peaks assigned to Eu^{2+} ions are usually located at 1156.4 and 1126.3 eV, respectively.[71] However, due to low concentration of europium dopant ion the analysis does not achieve good signal-to-noise and the presence of the Eu^{2+} can not be confirmed.

The adsorption–desorption isotherms for CeO_2 samples are presented in Fig. 5. All samples can be related with the typical IV isotherms with H1 hysteresis type. These isotherms are correlated to mesoporous particles (pores diameters ranging from 2 to 50 nm) with uniform pore size distribution.[9,72,73] The surface areas, pore diameters and pore volume values are shown in Table 2.

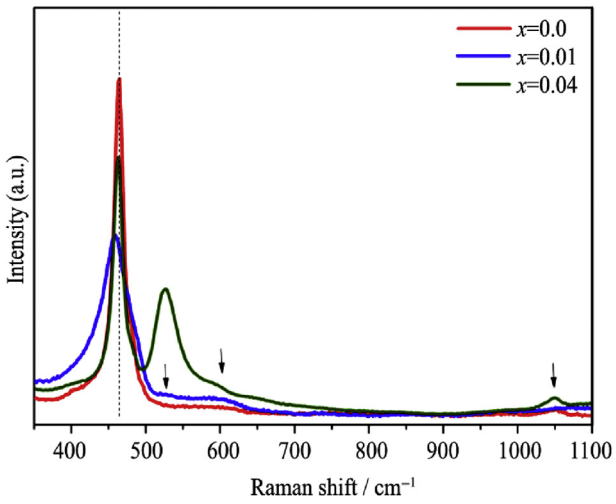

Fig. 3. Raman spectra of the $Ce_{1-x}Eu_xO_2$ samples (x = mol of Eu^{3+} ions).

presents higher surface area (163 m^2/g) when compared to the other CeO_2 samples. The pore volume for $Ce_{0.99}Eu_{0.01}O_2$ and $Ce_{0.96}Eu_{0.04}O_2$ samples is different, which may be due to high concentration of Eu^{3+} in the $Ce_{0.96}Eu_{0.04}O_2$. The surface area increases with a low dopant concentration in the lattice, however, high concentrations of dopant may block the pore of cerium oxide (due to the higher Eu^{3+} ratio in comparison to Ce^{4+}) and, consequently, the surface area and pore volume decrease, as reported by Chen and collaborators.[76]

3.2. Electrochemical studies

Electrochemical studies of CeO_2 samples were performed using the films deposited at graphite substrates. The electrochemical activity was investigated by cyclic voltammetry in 0.3 mol/L manganese sulfate in acid medium. The scan rate was 5.0 mV/s and potential range was 0.4–1.5 V. Cyclic voltammetry (CV) studies for graphite background was included for evaluate the deposition of CeO_2 at substrate. The application of manganese ions as electrolyte

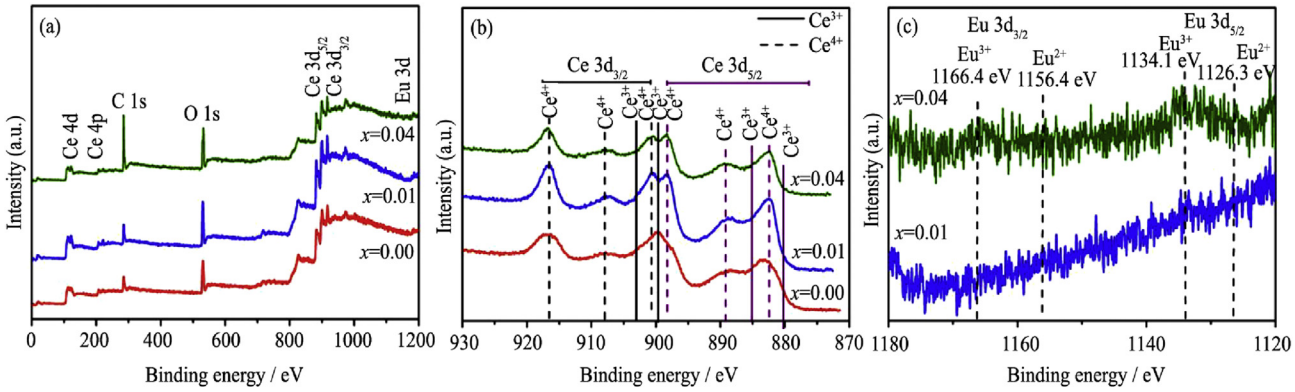

Fig. 4. XPS spectra (a), high-resolution Ce 3d XPS spectra (b) and Eu 3d XPS spectra for $Ce_{1-x}Eu_xO_2$ samples (x = mol of Eu^{3+} ions) (c).

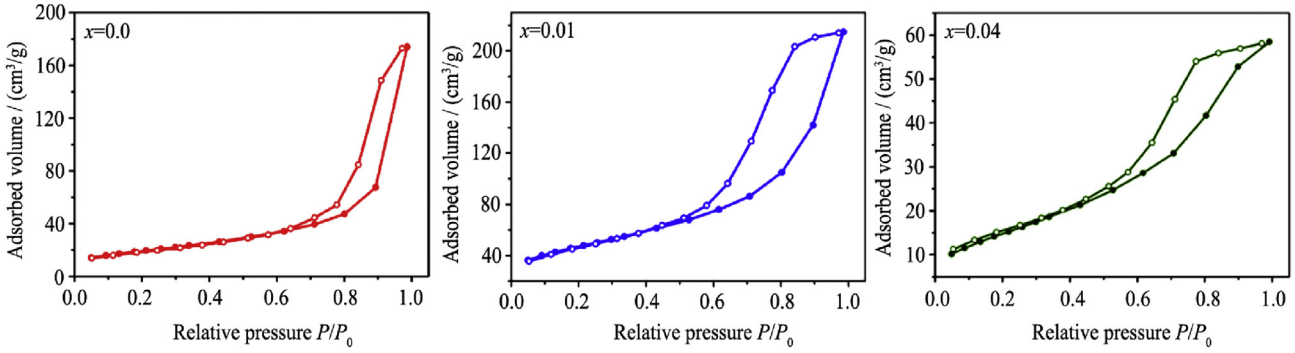

Fig. 5. N_2 adsorption/desorption isotherms of the $Ce_{1-x}Eu_xO_2$ samples (x = mol of Eu^{3+} ions).

The surface area values varied from 55 to 163 m^2/g. Small pore sizes and high pore volumes, usually, increase the surface area values.[74] Moreover, smaller particles have high surface areas due to elevated contact surface.[75] Table 2 shows that $Ce_{0.99}Eu_{0.01}O_2$

Table 2
Specific surface area and pore size data obtained for the $Ce_{1-x}Eu_xO_2$ samples (x = mol of Eu^{3+} ions).

Samples	S_{BET} (m^2/g)	D_{pore} (nm)	V_{pore} (cm^3/g)
0.0	69.24	11.48	0.274
0.01	163.51	6.64	0.333
0.04	55.53	6.64	0.093

in batteries is limited by Mn^{3+} ions disproportionation reaction (Eq. (1)).[36]

$$2Mn^{3+}_{(aq)} + 2H_2O_{(l)} \rightleftharpoons Mn^{2+}_{(aq)} + MnO_{2(s)} + 4H^+_{(aq)} \quad (1)$$

In aqueous solution, the Mn^{3+} ions are spontaneously converted into Mn^{2+} ions and manganese dioxide, which decreases the battery efficiency. High concentrations of H_2SO_4 were added in the system to move the equilibrium towards the formation of Mn^{3+} ions.[44] For this reason, we firstly evaluated the electrochemical profile of the different films in different sulfuric acid concentrations: 0.5, 1.0, 3.0

and 5.0 mol/L. The cyclic voltammograms for the $Ce_{1-x}Eu_xO_2$ films are shown in Fig. 6 and the respective data are presented in Table 3.

The voltammograms present a redox pair characteristic of the Mn^{2+}/Mn^{3+} redox couple. According to the results obtained from CV, all samples presented good redox reversibility (ΔE_p = 159–212 mV) and a regime of mass transport mainly controlled by diffusion, since the values of R^2, obtained by the I vs $v^{1/2}$ graph, were close to the unit (Fig. S1, Supporting Information). ΔE_p values for the same sample do not display great variations when H_2SO_4 concentration increased. However, it is possible to observe that the deposition of CeO_2 films (pure and doped with Eu^{3+}) on the graphite substrate increased the reversibility of redox process (taking into account the same acid concentration). In this work, we propose that CeO_2 acts as a catalyst by the electron transfer and reversible adsorption–desorption and intercalation-de-intercalation of Mn^{3+} and Mn^{2+} on the electrode surface.[77] The presence of intrinsic defects in $Ce_{1-x}Eu_xO_2$, such as oxygen vacancies as observed by Raman and, the coexistence of Ce^{4+} and Ce^{3+} ions confirmed by XPS measurements, increase the kinetics of redox reactions between Mn^{3+}/Mn^{2+}, which is in agreement with CVs data. Zhou and collaborators[26] reported a similar behavior when studying the addition of CeO_2 on graphite felt as electrode for vanadium redox flow batteries. They observed that the addition of CeO_2 on graphite felt increased the reversibility of VO^{2+}/VO_2^+ redox process and attributed this behavior to catalytic action of Ce^{4+}/Ce^{3+} redox pair along with high capacity to store and transport oxygen present in the CeO_2 structure deposited on the graphite surface.[26,78]

The high values of current peak ratio (i_{pa}/i_{pc}) indicate that the redox process is quasi-reversible for all the samples analyzed.

Table 3
CVs data of graphite substrate and $Ce_{1-x}Eu_xO_2$ films in different acid concentrations (x = mol of Eu^{3+} ions).

Acid concentration/(mol/L)		Samples			
		Graphite	x = 0.0	x = 0.01	x = 0.04
0.5	[a]ΔE_p	204	186	199	208
	i_{pa}	2.4	1.9	2.9	4.1
	i_{pc}	1.2	0.5	0.9	1.6
	i_{pa}/i_{pc}	2.1	3.5	3.2	2.6
1.0	ΔE_p	212	168	195	208
	i_{pa}	3.0	2.1	1.6	2.7
	i_{pc}	1.9	1.2	0.8	1.2
	i_{pa}/i_{pc}	1.6	1.7	2.0	2.2
3.0	ΔE_p	181	159	186	182
	i_{pa}	2.6	1.0	0.4	0.8
	i_{pc}	1.8	1.5	0.8	1.1
	i_{pa}/i_{pc}	1.4	0.6	0.4	0.7
5.0	ΔE_p	181	164	168	173
	i_{pa}	3.5	2.4	1.8	2.4
	i_{pc}	1.8	1.3	0.7	0.8
	i_{pa}/i_{pc}	2.0	1.8	2.7	3.2

[a] ΔE_p values in mV and i_{pa} and i_{pc} in mA/cm^2.

Therefore, considering the use of a low H_2SO_4 concentration (to avoid inhibition of the charge transfer due high viscosity), the good current intensity and ΔE_p values, all the further electrochemical activity measurements were performed using an aqueous solution of manganese sulfate (0.3 mol/L) and sulfuric acid (1.0 mol/L) as the electrolyte. Additionally, according to Xue and collaborators,[36] the absence of cathodic peak around 0.76 V, relative to MnO_2 presence, indicates once again that the use of CeO_2 films deposited on graphite

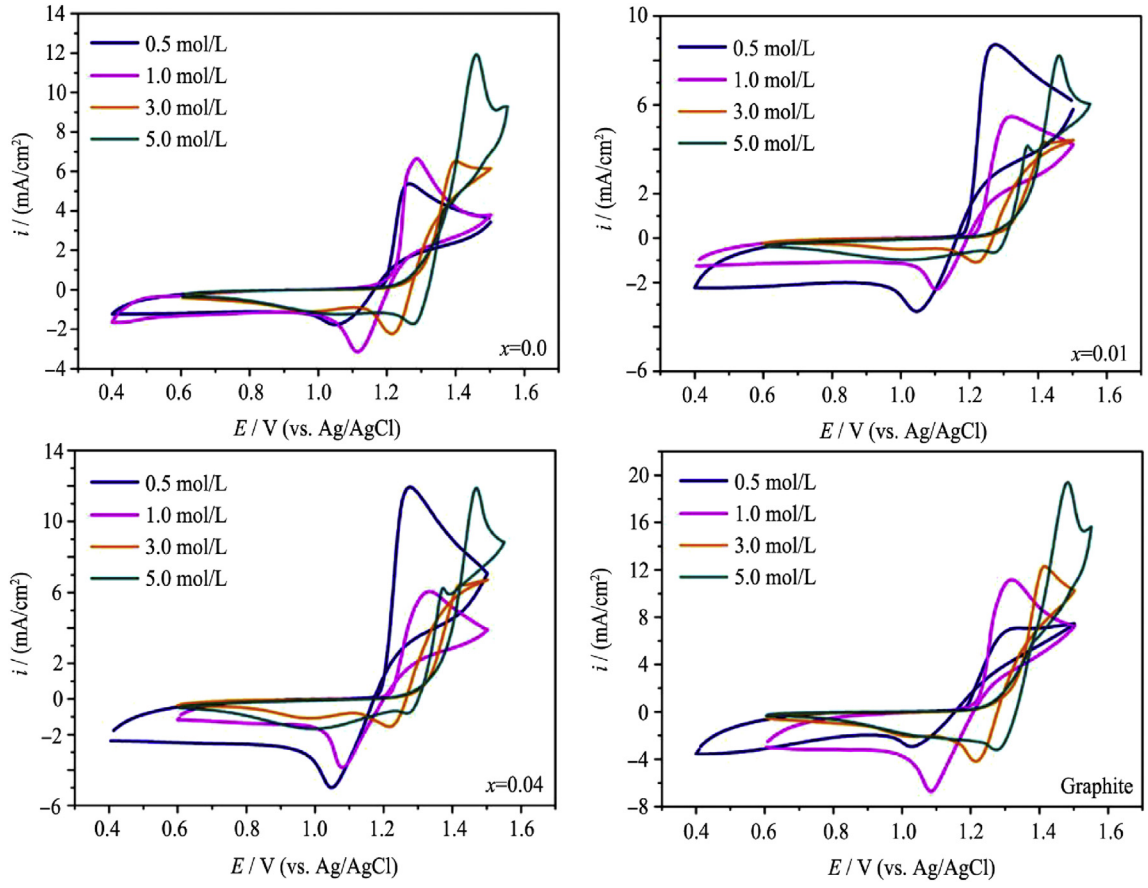

Fig. 6. Cyclic voltammograms of $Ce_{1-x}Eu_xO_2$ samples in $MnSO_4$ 0.3 mol/L in different H_2SO_4 concentrations at a scan rate of 5 mV/s (x = mol of Eu^{3+} ions).

electrodes in this pH value provided a control in the equilibrium of the reaction, avoiding the Mn^{3+} ions disproportionation reaction.

Galvanostatic charge–discharge tests (Fig. 7) were performed to evaluate the application of CeO_2 films as electrodes in manganese ions batteries.

Different values of current density (1.6, 2.0, 2.4, 2.8, 3.2, 3.6 and 8.0 mA/cm^2) were evaluated with the potential range of 0.9–1.5 V for each CeO_2 film. The results show that for lower current values the graphite substrate presents the best performance, however, when higher values of current density ($\geq$3.2 mA/cm^2) are applied the performance of CeO_2 films and $Ce_{0.99}Eu_{0.01}O_2$ increases considerably compared with the neat carbon substrate. However, $Ce_{0.96}Eu_{0.04}O_2$ presents lower electrochemical activity in all current density values. This behavior may be due to lower reversibility of redox process when compared to other CeO_2 films, in accordance to cyclic voltammogram results. These results may be associated to irreversible ion adsorption processes in this sample due to the higher quantity of defects, in according to Raman.

These results can be attributed to the excellent ion storage and transport properties of CeO_2, therefore, higher current density values can be associated with an increase in redox reaction kinetics (Ce^{4+}/Ce^{3+}). In addition, cerium oxide exhibits a pseudocapacitor electrochemical behavior, i.e., CeO_2 has the capacity to store energy through fast and reversible redox reactions which occur on the surface or near the surface of the nanoparticle deposited on the electrode.[77,79–81] This mechanism of energy storage is related to faradaic chemical processes, either by transfer of electrons or transport of ions. On the other hand, carbonaceous materials (e.g. graphite) provide the electrical double-layer formation by the accumulation of electrostatic charges on the electrode/electrolyte interface, constituting a non-faradaic process.[82,83]

The $Ce_{1-x}Eu_xO_2$ film addition on the graphite electrode surface promotes a synergistic effect between the energy storage mechanisms of both materials.[84] Thus, the electrical double-layer formation and the ionic transfer between the electrode and the electrolytic solution occur simultaneously, increasing the battery efficiency. For this reason, the presence of charged species in cerium oxide facilitates the electric double-layer charging and increases the storage and exchange of ions between the electrode surface and the electrolyte during the charge–discharge processes.[84]

Moreover, the deposition of CeO_2 nanoparticles in the form of a two-dimensional film structure can promote the fast ionic transport and dynamic processes. Furthermore, reorganizations in the surface of the oxides films may be responsible for this behavior, since the mobilization of CeO_2 particles to form films provides an accumulation of high density defects, with consequently large amount of active sites for ionic conduction.[85–87] Other possibility is the formation of a CeO_2-graphite composite, since several papers report an increase in electrochemical activity of oxides when associated with carbonaceous materials.[28,39,84,88] The comparison of different currents for the same sample was also performed and

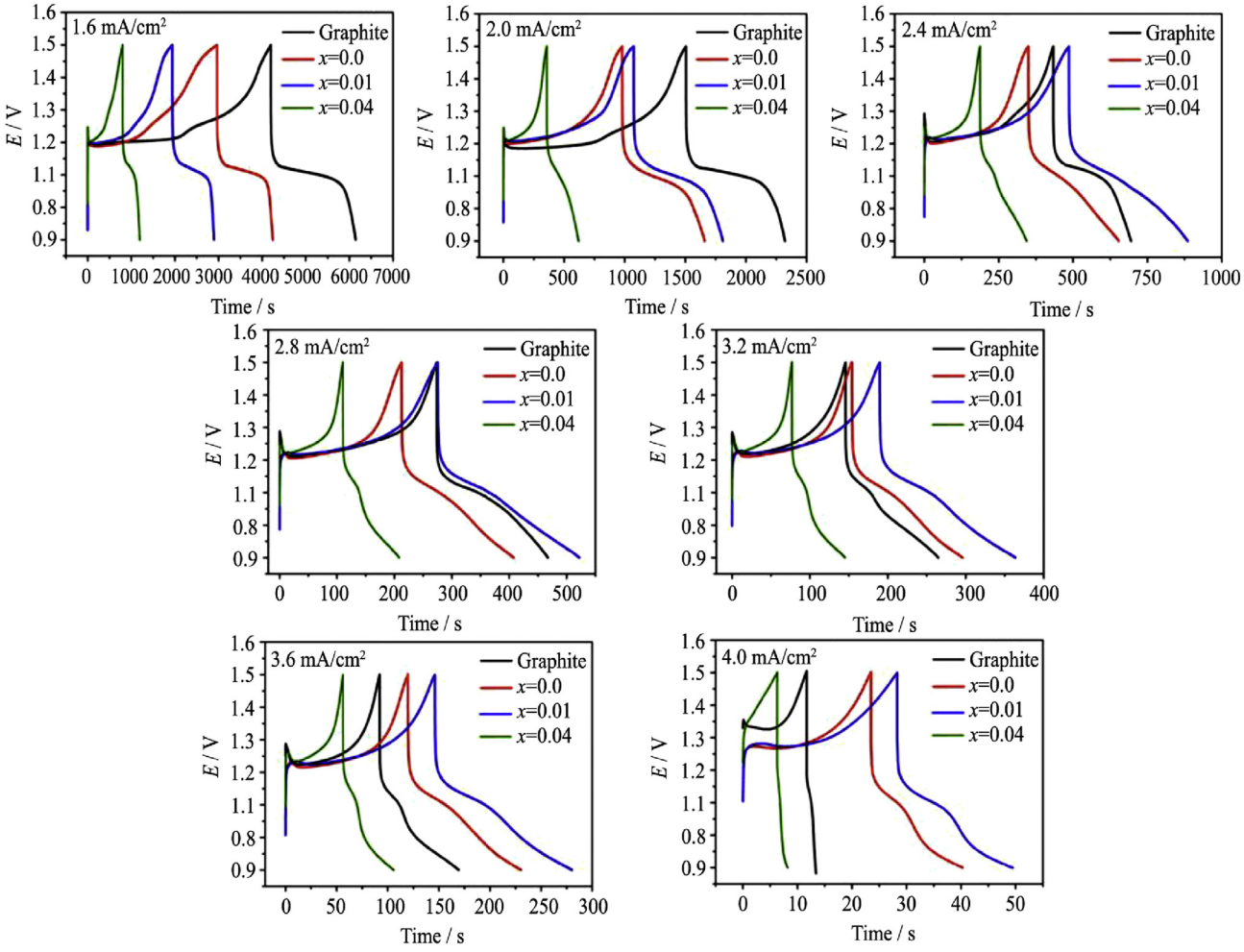

Fig. 7. Galvanostatic charge–discharge curves of the $Ce_{1-x}Eu_xO_2$ samples in $MnSO_4$ 0.3 mol/L and H_2SO_4 1.0 mol/L at potential range of 0.9–1.5 V (x = mol of Eu^{3+} ions).

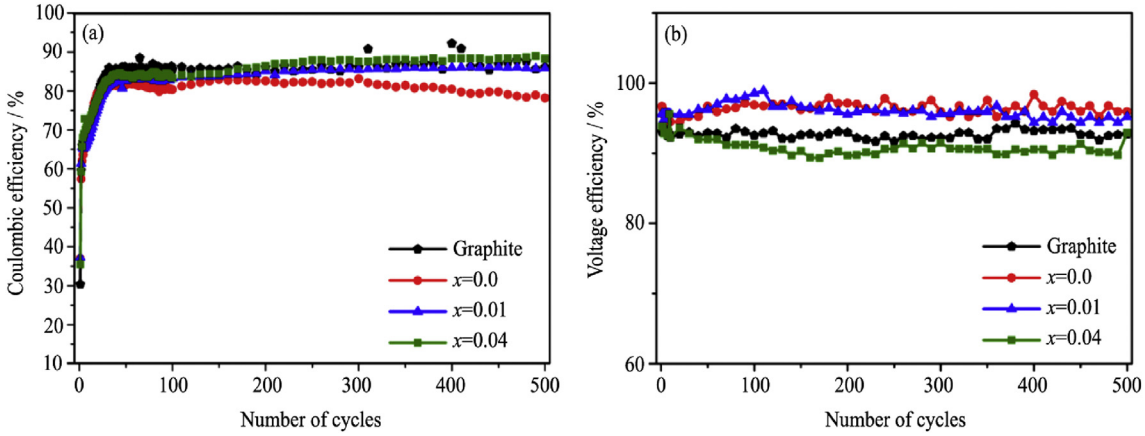

Fig. 8. Coulombic (a) and voltage efficiencies (b) of CeO_2 samples obtained from 500 galvanostatic charge–discharge cycles in $MnSO_4$ 0.3 mol/L and H_2SO_4 1.0 mol/L at potential range of 0.9–1.5 V.

specific capacity values were calculated for each current (Fig. S2 and Table S1, Supporting Information).

Stability tests for charge/discharge process were performed using a current density of 3.6 mA/cm^2 during 500 cycles (Fig. 8). All the films presented coulombic (8 (a)) higher than 80% and voltage efficiency (8 (b)) higher than 90% after 500 cycles. It is notable that the values of coulombic efficiency increased during the initial cycles, which indicates that the films go through an initial surface reorganization processes before efficient operation. This reorganization is related to irreversible process of ion adsorption at CeO_2 surface in first cycles, however, these process decrease during the charge–discharge cycle due to reduction of the charge transfer resistance, as reported by Ma and collaborators.[89]

These results are quite encouraging and CeO_2 films show to be very promising for application in batteries based on manganese ions. Galvanostatic charge–discharge tests performed using a current density of 3.6 mA/cm^2 showed that the $Ce_{0.99}Eu_{0.01}O_2$ film presents the best result, with specific capacity for the third cycle of 372.49 mAh/g compared with CeO_2 (334.84 mAh/g) and $Ce_{0.96}Eu_{0.04}O_2$ (75.15 mAh/g) films. However, when the Eu-doped samples were compared, $Ce_{0.96}Eu_{0.04}O_2$ film showed lower value of specific capacity, indicating that the electrochemical activity decreases with the increase of the dopant concentration. This fact can be assigned to Eu^{3+} excess in the film, which decreases the oxygen mobility in the structure.[90,91] Krishna and collaborators reported that higher storage and transport capacity of ions during redox process may be associated with an elevated volume of pores and consequently a more open structure of CeO_2 particles.[92] Li and collaborators[93] also reported that small mesopores and high surface areas facilitates mass and ion diffusion/transport, which may explain the higher electrochemical activity of $Ce_{0.99}Eu_{0.01}O_2$. These results corroborates with the surface area values obtained, since the best electrochemical performance was obtained for the sample that presented higher surface area and pore volume.

4. Conclusions

In summary, CeO_2 nanoparticles of hexagonal shape were successfully synthesized by microwave-hydrothermal method. According to XRD analysis and Raman spectroscopy, the Eu^{3+} ions were incorporated into CeO_2 matrix occupying the Ce^{4+} sites and generating oxygen vacancies. The coexistence of Ce^{4+}/Ce^{3+} ions in CeO_2 samples was confirmed by XPS measurements. Moreover, this redox pair acts as catalyst of Mn^{2+}/Mn^{3+} redox reaction. The samples exhibit high values of specific surface area. Galvanostatic charge–discharge tests indicate that electrochemical properties are dependent of the adsorption capacity of the samples and dopant concentration, with lower quantities of Eu^{3+} providing the best electrochemical results. CeO_2 films present different behaviors in different current densities which expands their electrochemical applications. High values of coulombic efficiency and specific capacity indicated that deposition of CeO_2 films at graphite substrates are promising systems for application in batteries based on manganese ions.

Acknowledgements

The authors are grateful to Coordenação de Aperfeiçoamento de Pessoal de Nível Superior (Capes), Conselho Nacional de Desenvolvimento Científico e Tecnológico (CNPq), Fundação de Amparo à Pesquisa do Estado de Minas Gerais (FAPEMIG), Rede Mineira de Química (RQ-MG) and Grupo de Materiais Inorgânicos do Triângulo – GMIT Research Group supported by FAPEMIG (APQ-00330-14) for the financial support. The authors would also like to thank Materials Chemistry Group at Federal University of Paraná for assistance in obtaining SEM images and to tank Multiuser Laboratory of the Institute of Physics at Federal University of Uberlândia for assistance in obtaining Raman data. The authors would like to thank Prof. Valmor R. Mastelaro for XPS measurements and Mr. Rorivaldo Camargo for the TEM analyses.

Appendix A. Supplementary data

Supplementary data related to this article can be found at https://doi.org/10.1016/j.jre.2018.05.004.

References

1. He LY, Su YM, Jiang LH, Shi SK. Recent advances of cerium oxide nanoparticles in synthesis, luminescence and biomedical studies: a review. *J Rare Earths*. 2015;33(8):791.
2. Mogensen M, Sammes NM, Tompsett GA. Physical, chemical and electrochemical properties of pure and doped ceria. *Solid State Ionics*. 2000;129(1):63.
3. Riccardi CS, Lima RC, dos Santos ML, Bueno PR, Varela JA, Longo E. Preparation of CeO_2 by a simple microwave-hydrothermal method. *Solid State Ionics*. 2009;180(2–3):288.
4. Campbell CT, Peden CH. Chemistry. Oxygen vacancies and catalysis on ceria surfaces. *Science*. 2005;309(5735):713.
5. de Rivas B, Guillén-Hurtado N, López-Fonseca R, Coloma-Pascual F, García-García A, Gutiérrez-Ortiz JI, et al. Activity, selectivity and stability of praseodymium-doped CeO_2 for chlorinated VOCs catalytic combustion. *Appl Catal B Environ*. 2012;121–122:162.

6. Fernandez-Garcia M, Martinez-Arias A, Hanson JC, Rodriguez JA. Nanostructured oxides in chemistry: characterization and properties. *Chem Rev*. 2004;104(9):4063.
7. Li L, Hu GS, Lu JQ, Luo MF. Review of oxygen vacancies in CeO_2-doped solid solutions as characterized by Raman spectroscopy. *Acta Phys Chim Sin*. 2012;28(5):1012.
8. Shi SK, Hossu M, Hall R, Chen W. Solution combustion synthesis, photoluminescence and X-ray luminescence of Eu-doped nanoceria CeO_2:Eu. *J Mater Chem*. 2012;22(44):23461.
9. Hernández WY, Laguna OH, Centeno MA, Odriozola JA. Structural and catalytic properties of lanthanide (La, Eu, Gd) doped ceria. *J Solid State Chem*. 2011;184(11):3014.
10. Fu JH, Xie W, Hu W, Zou LL, Qin N, Bao DH. Structure and photoluminescent properties of (200)-oriented Eu-doped CeO_2 thin films fabricated on fused silica substrates by chemical solution deposition. *Thin Solid Films*. 2014;573:100.
11. Tatar B, Gökdemir FP, Pehlivan E, Urgen M. The influence of Er^{3+} doping on the structural and optical properties of CeO_2 thin films grown by PED. *Appl Surf Sci*. 2013;285:409.
12. Vinodkumar T, Rao BG, Reddy BM. Influence of isovalent and aliovalent dopants on the reactivity of cerium oxide for catalytic applications. *Catal Today*. 2015;253:57.
13. Rovira LG, Delgado JJ, ElAmrani K, del Rio E, Chen X, Calvino JJ, et al. Synthesis of ceria-praseodimia nanotubes with high catalytic activity for CO oxidation. *Catal Today*. 2012;180(1):167.
14. Bera P, Gayen A, Hegde MS, Lalla NP, Spadaro L, Frusteri F, et al. Promoting effect of CeO_2 in combustion synthesized Pt/CeO_2 catalyst for CO oxidation. *J Phys Chem B*. 2003;107(25):6122.
15. Centi G, Perathoner S, Rak ZS. Reduction of greenhouse gas emissions by catalytic processes. *Appl Catal B Environ*. 2003;41(1–2):143.
16. Thakur S, Patil P. Rapid synthesis of cerium oxide nanoparticles with superior humidity-sensing performance. *Sensor Actuator B Chem*. 2014;194:260.
17. Rangaswamy A, Sudarsanam P, Reddy BM. Rare earth metal doped CeO_2-based catalytic materials for diesel soot oxidation at lower temperatures. *J Rare Earths*. 2015;33(11):1162.
18. Stojmenović M, Milenković MC, Banković PT, Žunić M, Gulicovski JJ, Pantić JR, et al. Influence of temperature and dopant concentration on structural, morphological and optical properties of nanometric $Ce_{1-x}Er_xO_{2-\delta}$ (x = 0.05–0.20) as a pigment. *Dyes Pigm*. 2015;123:116.
19. Qu XM, You LX, Tian XC, Zhang BW, Mahadevan GD, Jiang YX, et al. CeO_2 nanorods with high energy surfaces as electrocatalytical supports for methanol electrooxidation. *Electrochim Acta*. 2015;182:1078.
20. Zhang L, Shen Y. One-pot synthesis of platinum-ceria/graphene nanosheet as advanced electrocatalysts for alcohol oxidation. *ChemElectroChem*. 2015;2(6):887.
21. Liu HW, Liu HF. Preparing micro/nano dumbbell-shaped CeO_2 for high performance electrode materials. *J Alloys Compd*. 2016;681:342.
22. Padmanathan N, Selladurai S. Shape controlled synthesis of CeO_2 nanostructures for high performance supercapacitor electrodes. *RSC Adv*. 2014;4(13):6527.
23. Saravanan T, Shanmugam M, Anandan P, Azhagurajan M, Pazhanivel K, Arivanandhan M, et al. Facile synthesis of graphene-CeO_2 nanocomposites with enhanced electrochemical properties for supercapacitors. *Dalton Trans*. 2015;44(21):9901.
24. Manjunatha H, Suresh GS, Venkatesha TV. Electrode materials for aqueous rechargeable lithium batteries. *J Solid State Electrochem*. 2010;15(3):431.
25. Karl Chinnu M, Vijai Anand K, Mohan Kumar R, Alagesan T, Jayavel R. Synthesis and enhanced electrochemical properties of Sm:CeO_2 nanostructure by hydrothermal route. *Mater Lett*. 2013;113:170.
26. Zhou HP, Xi JY, Li ZH, Zhang ZY, Yu LH, Liu L, et al. CeO_2 decorated graphite felt as a high-performance electrode for vanadium redox flow batteries. *RSC Adv*. 2014;4(106):61912.
27. Cai GL, Yang YX, Guo RS, Zhang C, Wu C, Guo WN, et al. Synthesis and low temperature electrochemical properties of CeO_2 and C co-modified $Li_3V_2(PO_4)_3$ cathode materials for lithium-ion batteries. *Electrochim Acta*. 2015;174:1131.
28. Wu XY, Niu HL, Fu SS, Song JM, Mao CJ, Zhang SY, et al. Core-shell CeO_2@C nanospheres as enhanced anode materials for lithium ion batteries. *J Mater Chem A Mater Energy Sustain*. 2014;2(19):6790.
29. Michalska M, Hamankiewicz B, Ziółkowska D, Krajewski M, Lipińska L, Andrzejczuk M, et al. Influence of $LiMn_2O_4$ modification with CeO_2 on electrode performance. *Electrochim Acta*. 2014;136:286.
30. Liu HW, Le Q. Synthesis and performance of cerium oxide as anode materials for lithium ion batteries by a chemical precipitation method. *J Alloys Comp*. 2016;669:1.
31. Nava-Avendaño J, Arroyo-de Dompablo ME, Frontera C, Ayllón JA, Palacín MR. Study of sodium manganese fluorides as positive electrodes for Na-ion batteries. *Solid State Ionics*. 2015;278:106.
32. Sun J, Li JG, Zhou T, Yang K, Wei SP, Tang N, et al. Toxicity, a serious concern of thermal runaway from commercial Li-ion battery. *Nano Energy*. 2016;27:313.
33. Ordoñez J, Gago EJ, Girard A. Processes and technologies for the recycling and recovery of spent lithium-ion batteries. *Renew Sustain Energy Rev*. 2016;60:195.
34. Zhou Y, Wu XH, Wu WW, Wang KT. Synthesis and electrochemical performance of $Na_{0.7}Fe_{0.7}Mn_{0.3}O_2$ as a cathode material for Na-ion battery. *Ceram Int*. 2014;40(8):13679.
35. Fernández-Ropero AJ, Saurel D, Acebedo B, Rojo T, Casas-Cabanas M. Electrochemical characterization of $NaFePO_4$ as positive electrode in aqueous sodium-ion batteries. *J Power Sources*. 2015;291:40.
36. Xue FQ, Wang YL, Wang WH, Wang XD. Investigation on the electrode process of the Mn(II)/Mn(III) couple in redox flow battery. *Electrochim Acta*. 2008;53(22):6636.
37. Ding C, Zhang HM, Li XF, Liu T, Xing F. Vanadium flow battery for energy storage: prospects and challenges. *J Phys Chem Lett*. 2013;4(8):1281.
38. Jing MH, Wei ZF, Su W, He HX, Fan XZ, Qin Y, et al. Improved electrochemical performance for vanadium flow battery by optimizing the concentration of the electrolyte. *J Power Sources*. 2016;324:215.
39. Jing MH, Zhang XS, Fan XZ, Zhao LN, Liu JG, Yan CW. CeO_2 embedded electrospun carbon nanofibers as the advanced electrode with high effective surface area for vanadium flow battery. *Electrochim Acta*. 2016;215:57.
40. Barnard R, Baugh LM, Randell CF. The impedance of alkaline manganese cells and their relationship to cell performance. III. Correlation with high-rate pulse discharge capacity. *J Appl Electrochem*. 1987;17(1):185.
41. Yano M, Fujitani S, Nishio K, Akai Y, Kurimura M. Storage characteristics of mercury-free alkaline manganese batteries. *J Appl Electrochem*. 1998;28(11):1221.
42. Lipka SM, Swartz CR. *Hybrid flow battery and Mn/Mn electrolyte system. United States*. Lexington, KY (US): The University of Kentucky Research Foundation; 2016. PCT/US2012/039144.
43. Sleightholme AES, Shinkle AA, Liu Q, Li Y, Monroe CW, Thompson LT. Non-aqueous manganese acetylacetonate electrolyte for redox flow batteries. *J Power Sources*. 2011;196(13):5742.
44. He ZX, Jin GH, Gao C, Chen Y, Han HG, Liu JL. A new redox flow battery of high energy density with V/Mn hybrid redox couples. *J Renew Sustain Energy*. 2014;6(5):053124.
45. Romeiro FC, Marinho JZ, Silva AC, Cano NF, Dantas NO, Lima RC. Photoluminescence and magnetism in Mn^{2+}-doped ZnO nanostructures grown rapidly by the microwave hydrothermal method. *J Phys Chem C Nanomater Interfaces*. 2013;117(49):26222.
46. Araújo VD, Avansi W, de Carvalho HB, Moreira ML, Longo E, Ribeiro C, et al. CeO_2 nanoparticles synthesized by a microwave-assisted hydrothermal method: evolution from nanospheres to nanorods. *CrystEngComm*. 2012;14(3):1150.
47. Matei-Rutkovska F, Postole G, Rotaru CG, Florea M, Pârvulescu VI, Gelin P. Synthesis of ceria nanopowders by microwave-assisted hydrothermal method for dry reforming of methane. *Int J Hydrogen Energy*. 2016;41(4):2512.
48. Cabral AC, Cavalcante LS, Deus RC, Longo E, Simões AZ, Moura F. Photoluminescence properties of praseodymium doped cerium oxide nanocrystals. *Ceram Int*. 2014;40(3):4445.
49. Salvatierra RV, Oliveira MM, Zarbin AJG. One-pot synthesis and processing of transparent, conducting, and freestanding carbon nanotubes/polyaniline composite films. *Chem Mater*. 2010;22(18):5222.
50. Romeiro FC, Rodrigues MA, Silva LAJ, Catto AC, da Silva LF, Longo E, et al. rGO-ZnO nanocomposites for high electrocatalytic effect on water oxidation obtained by microwave-hydrothermal method. *Appl Surf Sci*. 2017;423:743.
51. Souza VHR, Husmann S, Neiva EGC, Lisboa FS, Lopes LC, Salvatierra RV, et al. Flexible, transparent and thin films of carbon nanomaterials as electrodes for electrochemical applications. *Electrochim Acta*. 2016;197:200.
52. Larson AC, Dreele RBV. *General structure analysis system (GSAS)*. Los Alamos National Laboratory Report LAUR. 2004.
53. Brunauer S, Emmett PH, Teller E. Adsorption of gases in multimolecular layers. *J Am Chem Soc*. 1938;60(2):309.
54. Barrett EP, Joyner LG, Halenda PP. The determination of pore volume and area distributions in porous substances. I. computations from nitrogen isotherms. *J Am Chem Soc*. 1951;73(1):373.
55. Pikalova EY, Murashkina AA, Maragou VI, Demin AK, Strekalovsky VN, Tsiakaras PE. CeO_2 based materials doped with lanthanides for applications in intermediate temperature electrochemical devices. *Int J Hydrogen Energy*. 2011;36(10):6175.
56. Sahoo SK, Mohapatra M, Anand S. Characterization and optical properties of Eu-doped cubic nano ceria synthesized by using the co-precipitation-hydrothermal route. *J Korea Phys Soc*. 2013;62(2):297.
57. Khan MAM, Khan W, Ahamed M, Alhazaa AN. Microstructural properties and enhanced photocatalytic performance of Zn doped CeO_2 nanocrystals. *Sci Rep*. 2017;7(1):12560.
58. Vinothkumar G, Amalraj R, Babu KS. Fuel-oxidizer ratio tuned luminescence properties of combustion synthesized europium doped cerium oxide nanoparticles and its effect on antioxidant properties. *Ceram Int*. 2017;43(7):5457.
59. Shannon RD. Revised effective ionic radii and systematic studies of interatomic distances in halides and chalcogenides. *Acta Crystallogr A Found Adv*. 1976;32(5):751.
60. Zhao L, Perry NH, Sasaki K, Bishop SR. Electronic and ionic conductivity of $Eu_{0.2}Ce_{0.8}O_{2-\delta}$. *Solid State Ionics*. 2014;263:75.
61. Bonamartini Corradi A, Bondioli F, Ferrari AM, Manfredini T. Synthesis and characterization of nanosized ceria powders by microwave-hydrothermal method. *Mater Res Bull*. 2006;41(1):38.
62. Bondioli F, Ferrari AM, Lusvarghi L, Manfredini T, Nannarone S, Pasquali L, et al. Synthesis and characterization of praseodymium-doped ceria powders by a microwave-assisted hydrothermal (MH) route. *J Mater Chem*. 2005;15(10):1061.
63. Bezkrovnyi OS, Lisiecki R, Kepinski L. Relationship between morphology and structure of shape-controlled CeO_2 nanocrystals synthesized by microwave-assisted hydrothermal method. *Cryst Res Technol*. 2016;51(10):554.

64. Dos Santos ML, Lima RC, Riccardi CS, Tranquilin RL, Bueno PR, Varela JA, et al. Preparation and characterization of ceria nanospheres by microwave-hydrothermal method. *Mater Lett*. 2008;62(30):4509.
65. Mandal BP, Roy M, Grover V, Tyagi AK. X-ray diffraction, μ-Raman spectroscopic studies on CeO_2–RE_2O_3 (RE=Ho, Er) systems: observation of parasitic phases. *J Appl Phys*. 2008;103(3):033506.
66. Weber WH, Hass KC, McBride JR. Raman study of CeO_2: second-order scattering, lattice dynamics, and particle-size effects. *Phys Rev B*. 1993;48(1):178.
67. McBride JR, Hass KC, Poindexter BD, Weber WH. Raman and X-ray studies of $Ce_{1-x}RE_xO_{2-y}$, where RE=La, Pr, Nd, Eu, Gd, and Tb. *J Appl Phys*. 1994;76(4):2435.
68. Nakajima A, Yoshihara A, Ishigame M. Defect-induced Raman spectra in doped CeO_2. *Phys Rev B*. 1994;50(18):13297.
69. Polyak Y, Bastl Z. XPS and factor analysis study of initial stages of cerium oxide growth on polycrystalline tungsten. *Surf Interface Anal*. 2015;47(6):663.
70. Song XY, Ma Y, Ge X, Zhou HJ, Wang GZ, Zhang HM, et al. Europium-based infinite coordination polymer nanospheres as an effective fluorescence probe for phosphate sensing. *RSC Adv*. 2017;7(14):8661.
71. Kim D, Jin YH, Jeon KW, Kim S, Kim SJ, Han OH, et al. Blue-silica by Eu^{2+}-activator occupied in interstitial sites. *RSC Adv*. 2015;5(91):74790.
72. Kruk M, Jaroniec M. Gas adsorption characterization of ordered organic-inorganic nanocomposite materials. *Chem Mater*. 2001;13(10):3169.
73. Gregg SJ, Sing KSW. *Adsorption, surface area and porosity*. London: Academic Press; 1982.
74. Szabó Z, Ohmacht R, Huck CW, Stöggl WM, Bonn GK. Influence of the pore structure on the properties of silica based reversed phase packings for LC. *J Separ Sci*. 2005;28(4):313.
75. Khan ME, Khan MM, Cho MH. Ce^{3+}-ion, surface oxygen vacancy, and visible light-induced photocatalytic dye degradation and photocapacitive performance of CeO_2-graphene nanostructures. *Sci Rep*. 2017;7(1):5928.
76. Chen GX, Li QL, Wei YC, Fang WP, Yang YQ. Low temperature CO oxidation on Ni-promoted CuO-CeO_2 catalysts. *Chin J Catal*. 2013;34(2):322.
77. Maiti S, Pramanik A, Mahanty S. Extraordinarily high pseudocapacitance of metal organic framework derived nanostructured cerium oxide. *Chem Commun (Camb)*. 2014;50(79):11717.
78. Zhang ZH, Liu J, Gu JJ, Su L, Cheng LF. An overview of metal oxide materials as electrocatalysts and supports for polymer electrolyte fuel cells. *Energy Environ Sci*. 2014;7(8):2535.
79. Augustyn V, Simon P, Dunn B. Pseudocapacitive oxide materials for high-rate electrochemical energy storage. *Energy Environ Sci*. 2014;7(5):1597.
80. Murugan R, Ravi G, Vijayaprasath G, Rajendran S, Thaiyan M, Nallappan M, et al. Ni-CeO_2 spherical nanostructures for magnetic and electrochemical supercapacitor applications. *Phys Chem Chem Phys*. 2017;19(6):4396.
81. Zheng SS, Li XR, Yan BY, Hu Q, Xu YX, Xiao X, et al. Transition-metal (Fe, Co, Ni) based metal-organic frameworks for electrochemical energy storage. *Adv Energy Mater*. 2017;7(18):1602733.
82. Meyendorf NG, Shuvo MAI, Karim H, Islam MT, Rodriguez G, Nandasiri MI, et al. High-performance porous carbon/CeO_2 nanoparticles hybrid super-capacitors for energy storage. *Proc SPIE*. 2015;9439:94390H.
83. Guo XT, Zheng SS, Zhang GX, Xiao X, Li XR, Xu YX, et al. Nanostructured graphene-based materials for flexible energy storage. *Energy Storage Mater*. 2017;9:150.
84. Enterría M, Gonçalves AG, Pereira MFR, Martins JI, Figueiredo JL. Electrochemical storage mechanisms in non-stoichiometric cerium oxide/multiwalled carbon nanotube composites. *Electrochim Acta*. 2016;209:25.
85. Zhu B, Xia CR, Luo X, Niklasson G. Transparent two-phase composite oxide thin films with high conductivity. *Thin Solid Films*. 2001;385:209.
86. Li B, Gu P, Feng YC, Zhang GX, Huang KS, Xue HG, et al. Ultrathin nickel-cobalt phosphate 2d nanosheets for electrochemical energy storage under aqueous/solid-state electrolyte. *Adv Funct Mater*. 2017;27(12):1605784.
87. Xiao X, Zheng SS, Li XR, Zhang GX, Guo XT, Xue HG, et al. Facile synthesis of ultrathin Ni-MOF nanobelts for high-efficiency determination of glucose in human serum. *J Mater Chem B*. 2017;5(26):5234.
88. Li H, Nie JC, Kunsági-Máté S. EtOH induced formation of nanographite fractions and their reorganization on nanostructured CeO_2 films. *Chem Phys Lett*. 2012;531:183.
89. Ma MB, Wang HJ, Liang S, Guo SW, Zhang Y, Du XF. Porous carbon-wrapped cerium oxide hollow spheres synthesized via microwave hydrothermal for long-cycle and high-rate lithium-ion batteries. *Electrochim Acta*. 2017;256:110.
90. Mogensen M, Lindegaard T, Hansen UR, Mogensen G. Physical properties of mixed conductor solid oxide fuel cell anodes of doped CeO_2. *J Electrochem Soc*. 1994;141(8):2122.
91. Shuk P, Greenblatt M, Croft M. Hydrothermal synthesis and properties of $Ce_{1-x}Eu_xO_{2-\delta}$ solid solutions. *J Alloys Compd*. 2000;303:465.
92. Krishna K, Bueno-López A, Makkee M, Moulijn JA. Potential rare earth modified CeO_2 catalysts for soot oxidation. *Appl Catal B Environ*. 2007;75(3–4):189.
93. Li XR, Xue HG, Pang H. Facile synthesis and shape evolution of well-defined phosphotungstic acid potassium nanocrystals as a highly efficient visible-light-driven photocatalyst. *Nanoscale*. 2017;9(1):216.